ACS OMEGA

http://pubs.acs.org/journal/acsodf

Article

Simulation Investigation on the Structure and Its Influence on the Impinging Pressure of the Carbon Dioxide Jet

Chao Pu, Zhenjian Liu,* and Ge Pu

Cite This: *ACS Omega* 2023, 8, 25326−25335

Read Online

ACCESS | Metrics & More | Article Recommendations

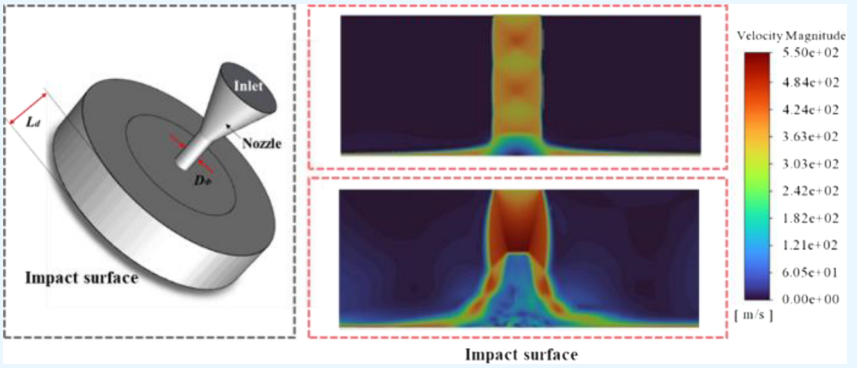

ABSTRACT: An improved understanding of the mechanisms of SC-CO_2 jet drilling technology is important for the application of this new technology. The flow field structure and dynamic fluctuation of SC-CO_2 jets are the key factors affecting the jet erosion performance. To improve the erosion performance of the SC-CO_2 jet, it is necessary to study the relationship between the different flow fields of the jet. In this study, a numerical simulation model for SC-CO_2 jet drilling technology is established. Based on the modified real-gas model, the pressure distribution and flow field characteristics of the SC-CO_2 jet were obtained by the simulation investigation, and the reliability of the model was verified. The results show that the flow field structure of a supercritical CO_2 jet has typical compressible flow field characteristics. As the jet is fully expanded, its pressure fluctuation is slight and less affected by the distance between the nozzle and the wall. When the jet is in the state of under-expansion, the flow field structure characteristics have a significant impact on the pressure distribution and peak pressure. At the same time, when the distance is large, when nozzle pressure ratio = 5, the pressure ratio has a more significant impact on the flow field and the pressure peak and distribution. The pressure distribution of different flow fields should be fully considered in the application.

1. INTRODUCTION

With the global reduction of natural gas resources, a significant portion of natural gas will be supplied by unconventional natural gas in the future.[1−3] Unconventional natural gas, represented by tight gas, shale gas, and coalbed methane (CBM), has attracted widespread concern due to its huge resource potential. CBM, which is inherent to coal and is formed during coalification, has attracted worldwide attention. With the increase in energy demand and the extension of mining depth, the low formation permeability seriously restricts the transportation of unconventional natural gas trapped to the vertical production wells.[4] Thereby, improving the permeability of unconventional natural gas reserves has become an urgent issue. Over the last few years, there have been numerous research studies with respect to methods to improve the efficiency of unconventional natural gas extraction, among which hydraulic fracturing is the most widely used stimulating technology in unconventional natural gas extraction.[5−9] However, some disadvantages still exist, which may hinder the widespread application of this technology. For instance, the consumption of fresh water may result in waste of water resources and may lead to formation permeability damage.[10] As a result, waterless stimulation techniques are still in demand to reduce water requirements and minimize environmental impacts. As a new waterless stimulation technique, SC-CO_2 jet drilling technology, as shown in Figure 1, has excellent potential for drilling of its incomparable advantages. Compared to hydraulic fracturing, SC-CO_2 can produce more fracture initiation and propagation cracks at lower pressures.[11,12] In the process of CO_2 injection, CO_2 is in the supercritical state in the initial state. SC-CO_2 has unique

Received: April 21, 2023
Accepted: June 28, 2023
Published: July 9, 2023

https://doi.org/10.1021/acsomega.3c02751
ACS Omega 2023, 8, 25326−25335

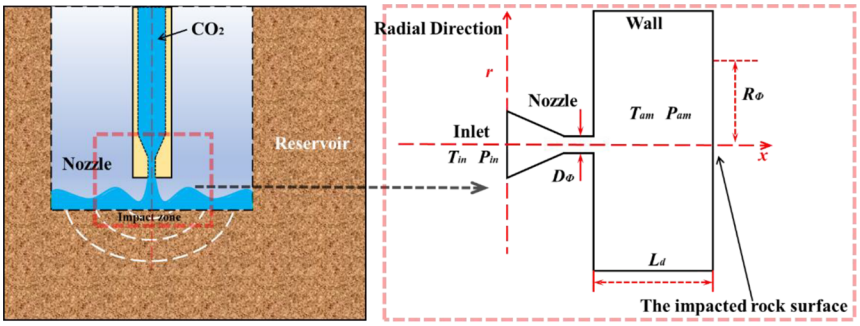

Figure 1. Schematic diagram: (a) CO_2 jet process; (b) sketch of the computational domain and configuration of the nozzle.

physical properties, such as gas-like viscosity and flow properties coupled with liquid-like density and dissolution power, thus reducing the pressure loss during the drilling process and little residual fracturing SC-CO_2 left in reservoirs preventing damage to the permeability.[13] The thermophysical parameters of SC-CO_2 in the whole process are sensitive to pressure and temperature variations that may result in complex fluid flow and heat transfer. The improvement of its efficiency in gas recovery is still a huge challenge, and further research is still needed.[14−16]

The impinging pressure and the flow field structure are the two key factors influencing the efficiency of SC-CO_2 impinging jet rock-breaking.[5,13,17,18] Specifically, the high-pressure CO_2 jets at the bottom are often in an under-expanded state. The impinging jet involves the occurrence of the shock structure. The shock structures will significantly change the flow characteristics, as well as the pressure distribution.[19] For the under-expanded jet, previous research shows that the maximum pressure does not occur at the center of the plate and that a region of reversed flow exists near the center of the plate.[20,21] Therefore, studying the effect of different fluid flow structures on rock-breaking efficiency is essential, especially for conditions such as the distance between the nozzle to the target and the nozzle pressure ratio (NPR). For instance, Zhang et al.[6] investigated the fluctuation characteristics and its flow field influence on the impact force of supercritical carbon dioxide jets. Their results indicate that the flow field and the stagnation point position significantly affected the impinging pressure where the pressure in the compression wave is higher than that at the expansion position. Tian et al.[8] investigated the influences of the ambient pressure and the nozzle-to-target distance on the jet-impinging pressure. They concluded that the depth of the perforation hole and volume decreased as the nozzle-to-target distance extended, while the impinging hole depth decays substantially when the distance exceeds a certain critical point. Liu et al.[14] reported that the differential pressure ratio mainly affects the SC-CO_2 jet flow field structure. The flow field structure is more conducive to controlling the flow field and improving rock-breaking efficiency when the jet is under-expanded. The result showed the best results when the pressure ratio was 1.31. It can be concluded from these studies that the different flow field structures may significantly influence the pressure distribution, thus affecting the rock-breaking efficiency. The flow field structure is determined by many factors, e.g., the distance between nozzles, the environment, inlet pressure, etc. Recent research demonstrated that there is an optimal nozzle-to-wall distance under low ambient pressure, and reducing the nozzle-to-wall distance is better for fracturing under high ambient pressure.[15] For the complex flow field structure on the wells and external influence factors, the influence of different flow field structures on the rock-breaking has not been fully established, and further analysis is warranted.

In addition, due to the oscillation of the shock wave and the feedback effect on the flow field, fluctuations in pressure are caused by the impinging surface of the target. The pressure fluctuation characteristics on the surface of the plate were also observed for under-expansion shocks, indicating the pressure fluctuations induced by a compressible jet flow.[22−25] The flow field analysis of the impinging jets has been studied extensively, where their characterization has been used in many engineering applications.[26] Yaga et al.[27] found that stagnation pressure on the plate depends on the pressure in the chamber and the distance between the nozzle to the plate. The pressure distributions on the impinging plate are nonaxisymmetric. Chin et al.[28] numerically investigated the compressible impinging at various impinging angles and nozzle-to-wall distances. They concluded that impinging wall significantly affects the shock structures when the nondimensional nozzle-to-wall distance is less than 1.5. As a result, the shock structure of the cell from fully developing increases the Mach disk size. So far, however, there has been little discussion about the fluctuating characteristics and the effect of its under-expanded flow field structure, particularly in the study of rock-breaking.

Due to the high pressure and temperature levels, developing direct experimental approaches for observing the pressure and flow field is challenging. Computational fluid dynamics (CFD) has been deemed as a valuable method for studying the flow field of the under-expanded SC-CO_2 jet. For the simulation of the SC-CO_2 jet, both the equation of state (EOS) and the choice of simulation method are key parameters for the accuracy of the result.[29] For instance, Zhang et al.[24] have established a numerical model to investigate the dynamic oscillation characteristics of SC-CO_2 by using a standard $k-\varepsilon$ turbulence model. Wang et al.[30] used the Peng−Robinson EOS to compute the thermodynamic properties and the structure of the under-expanded jet of CO_2. The SST $k-\omega$ turbulence model was used in the research. For the under-expanded CO_2 jet, the simulation result showed that the SST $k-\varepsilon$ model could predict the structure of the flow field more accurately than the $k-\varepsilon$ model. The SST $k-\varepsilon$ model performs better in resolving the detailed flow structure and predicting the velocity, as reported by Liu et al.[31] Compared to the Reynolds-averaged Navier−Stokes (RANS), large-eddy simulation (LES) and detached-eddy simulation DES reproduces the turbulent dynamics in the shear layer more accurately, thereby better predicting the flow field of the impinging jet. Using DES, Wu et al.[32] investigated the flow field and heat

https://doi.org/10.1021/acsomega.3c02751
ACS Omega 2023, 8, 25326−25335

transfer in cryogenic nitrogen jets. The result reveals the prevailing role of large-scale vortices in heat transfer. The simulation can predict the temperature fluctuation of the stagnation point very well. Kubacki[33] indicated round impinging jet heat transfer with two $k-\omega$ hybrid RANS/LES models. All models reproduce the mean velocity distribution well at the shorter nozzle-to-plate distance. For more considerable nozzle-to-plate distances, the hybrid model produces the jet region's mean and fluctuating velocity distributions very well. The RANS results have significant errors due to the inaccurate jet shear layer mixing prediction. Gojon and Bogey[34] conducted a computational study of the under-expanded jet at a high NPR. The result indicates that the near-field structures captured by the LES were in good agreement with the experiments. The research shows that the DES approach performs significantly better in predicting the flow field of impinging jets than the widely used $k-\varepsilon$-based RANS method.[32] Raman and Kim[35] analyzed the influence of EOS selection on SC-CO_2 modeling using six EOS candidates. Their results showed that the shock-wave forms are susceptible to the different EOSs. Wang et al.[36] found that the real gas EOS was considerably superior to the ideal gas EOS in predicting the near-field temperatures of CO_2 jets. The choice of EOS is also crucial at high pressure for simulation because the thermodynamic properties of CO_2 may change significantly as the temperature and pressure change slightly.

The research aimed to elucidate the effects of pressure fluctuations and the structure of the flow field in supercritical CO_2 jet on rock-breaking efficiency. The DES approach was used for the simulation. The impinging jets of different distances were simulated based on the DES approach and the Span and Wagner (S−W) EOS. Effects of critical parameters, such as inlet pressure, were also analyzed. The results are expected to provide a theoretical basis and reference for developing SC-CO_2 jet technology.

2. METHODS AND MODELS

2.1. Real Gas Model. Accurately calculating the thermodynamic properties of SC-CO_2 during the whole process is the key prerequisite to the simulation. In this simulation of the entire process of SC-CO_2 flow through the nozzle and impinging the rock, real-gas EOS is used to satisfy this requirement. In the trans-critical state, the state parameters of CO_2 vary drastically. The required physical parameters can be accurately obtained using the S−W state equation, an accurate EOS used by a semi-analytical approach. The standard software provides built-in EOSs, such as critical EOSs and more complex EOSs from the NIST REFPROP. The state equation of S−W, as found in the relevant literature, predicts the properties of CO_2 with higher accuracy in gaseous and supercritical states. The S−W EOS[37] is described by:

$$\frac{A(\rho, T)}{RT} = \varphi(\delta, \tau) = \varphi^0(\delta, \tau) + \varphi^\gamma(\delta, \tau) \quad (1)$$

T_c is the critical point temperature of CO_2 and ρ_c is the density of CO_2 at the critical point. Where $\delta = \rho/\rho_c$ and $\tau = T_c/T$, with ρ_c = 467.6 kg/m^3 and T_c = 304.13 K. The formulations that describe the Helmholtz energy's ideal-gas energy are given in eq 2, and the residual part of the Helmholtz energy is in eq. 3:

$$\phi^0(\delta, \tau) = \ln(\delta) + a_1^0 + a_2^0\tau + a_3^0\ln(\tau) + \sum_{i=4}^{8} a_i^0 \ln[1 - \exp(-\tau\theta_i^0)] \quad (2)$$

$$\phi^\tau(\delta, \tau) = \sum_{i=1}^{7} n_i\delta^{d_i}\tau^{d_i} + \sum_{i=8}^{34} n_i\delta^{d_i}\tau^{d_i}e^{-\delta^{c_i}} + \sum_{i=35}^{39} n_i\delta^{d_i}\tau^{d_i}e^{-a_i(\delta-\varepsilon_i)^2} + \sum_{i=40}^{42} n_i\Delta^{b_i}\delta e^{-c_i(\delta-1)^2-D_i(\tau-1)^2} \quad (3)$$

In the formulation, the Δ is defined as:

$$\Delta = \{(1-\tau) + A_i[(\delta-1)^2]^{1/(2\beta_i)}\}^2 + B_i[(\delta-1)^2]^{a_i} \quad (4)$$

δ is the (dimensionless) density, and τ is the (dimensionless) temperature. The coefficients a_i^0 and θ_i^0 are given in Table 1.

Table 1. Coefficients of the Correlation Equations in eq 2

i	a_i^0	θ_i^0
1	8.37304456	
2	−3.70454304	
3	2.50000000	
4	1.99427042	3.15163
5	0.62105248	6.11190
6	0.41195293	6.77708
7	1.04028922	11.32384
8	0.08327678	27.08792

2.2. Computational Simulation Domain and Boundary Conditions. Several geometry-impinging jet models were set up in the present study. Figure 2 demonstrates the three-dimensional geometric model for the jet simulation. Based on the jet's process features, two geometric models were established using simplified conditions for the flow field. The nozzle domain of the models is the same. The diameter of the CO_2 jet nozzle D_Φ is 2 mm. The dimensionless jet stand-off distance (L_d/D_Φ) and radial distance (R/r) are defined as the ratio of stand-off distance to D_Φ (nozzle diameter) and radial distance to r (nozzle radius), respectively. The detailed model information is shown in Figure 2. The stand-off distance L_d varies from 6 to 10 mm in the imping jet model. The inlet pressure of the nozzle is denoted by P_{in}, and P_{am} denoted outlet pressure. The pressure ratio (NPR)

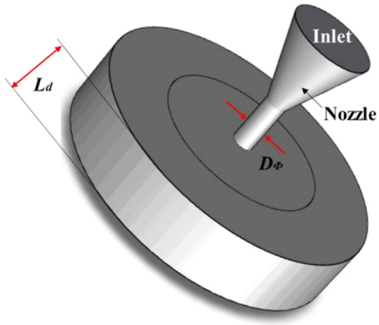

Figure 2. Geometry model for the simulation.

https://doi.org/10.1021/acsomega.3c02751
ACS Omega 2023, 8, 25326−25335

of the nozzle is defined as the ratio of inlet pressure P_{in} to ambient pressure P_{am}.

To ensure convergence, the location of the large velocity gradient is refined. The total number of grids was set as 3.2 million. Due to the flow properties of CO_2, different mesh densities were set for the various regions. To improve the calculation computational efficiency while accurately capturing the complex turbulence characteristics of the jet, a high-density mesh was generated in the area within the shear layer of the jet and the impinging region.

In addition, grid independence was utilized to ensure the accuracy. As shown in Figure 3, when the grid size increased

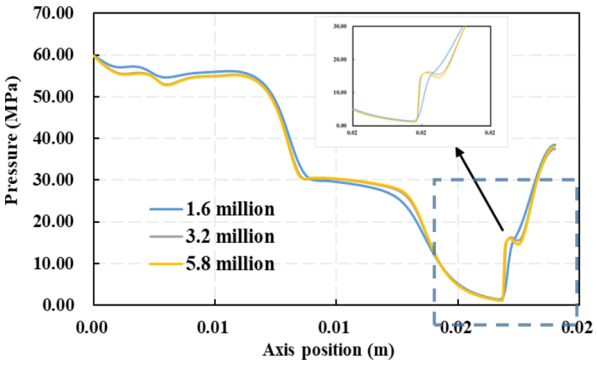

Figure 3. Pressure, along with the axis profile, as a function of the number of grid cells.

from 3.2 million to 5.8 million cells, the pressure along the axis profile showed only a tiny deviation, and the details were captured accurately. Therefore, a grid size of 3.2 million was considered sufficient for this study.

2.3. Governing Equations and Turbulence Model of the Simulation. As a compressible flow fluid, thus, the continuity, momentum, and energy equations must be solved in the simulation. In addition, this study assumes that the influence of gravity can be ignored. The equation can be expressed as follows:

$$\frac{\partial \rho}{\partial t} + \frac{\partial(\rho v_i)}{\partial x_i} = 0 \tag{5}$$

$$\frac{\partial(\rho v_i)}{\partial t} + \frac{\partial(\rho v_i v_j)}{\partial x_j} = -\frac{\partial p}{\partial x_i} + \frac{\partial}{\partial x_j}\left(\mu \frac{\partial v_i}{\partial x_j}\right) + S_i \tag{6}$$

where p is the static pressure, t denotes time, ρ denotes density, and x_i represents the ith coordinate (i = 1, 2, 3). For the SST $k-\omega$ model,

$$\frac{\partial}{\partial t}(\rho k) + \frac{\partial}{\partial x_i}(\rho k u_i) = \frac{\partial}{\partial x_j}\left(\Gamma_k \frac{\partial k}{\partial x_j}\right) + G_k - Y_k + S_k \tag{7}$$

$$\frac{\partial}{\partial t}(\rho w) + \frac{\partial}{\partial x_i}(\rho w u_i) = \frac{\partial}{\partial x_j}\left(\Gamma_k \frac{\partial w}{\partial x_j}\right) + G_w - Y_w + D_w + S_w \tag{8}$$

where G_k represents the generation of turbulence kinetic energy, and G_w represents the generation of w. Γ_k and Γ_w represent the effective diffusivity of k and w.

In the DES model, the dissipation term of the turbulent kinetic energy is modified for the DES turbulence model such as:

$$Y_k = \rho\beta^* k\omega F_{DES} \tag{9}$$

where F_{DES} is expressed as

$$F_{DES} = \max\left(\frac{L_t}{C_{DES}\Delta_{max}}, 1\right) \tag{10}$$

where C_{DES} is a calibration constant used in the model, and the value is 0.61. Δ_{max} is the grid spacing, which is the maximum edge length in the case of a rectilinear hexahedral cell.

2.4. Simulation Methodology. To further improve the accuracy, the model's propulsion solution speed should be larger than the actual physical disturbance propagation speed to obtain the small vortex structure at a small scale. In this study, the simulation time step Δt is set to 1×10^{-7} s, which can achieve simulation accuracy well. The solver used the double-precision density-based coupled solver. No-slip velocity and adiabatic boundary conditions were set at the wall boundaries. The semi-implicit method for pressure-linked equations *SIMPLE* segmentation algorithm was used to obtain the coupling of multiple fields. A third-order implicit scheme was used for temporal discretization.

3. RESULTS AND DISCUSSION

3.1. Model Verification. In order to verify the accuracy of the calculation model, the experimental data reported by Zhou et al.[7] were used to validate the computational procedure. The simulation results of the pressure distribution with the geometric model are shown in Figure 4. The experiments described in the

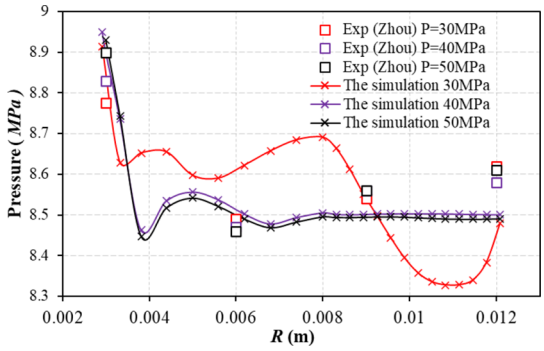

Figure 4. Comparison of the experimental and simulation results.

paper used a simulated real well bottom environment with measurement points set in a 3−12 mm arrangement with an interval of 3 mm. The distance from the nozzle outlet to the measurement plate is set to 6 mm. The experiment case of 30 to 50 MPa was compared with the current simulation results. The ambient pressure in the simulation was set to 8.5 MPa, which is in accordance with the experimental data. The pressure distribution adopts the value compared with the experimental data and the simulation result. The average error between the simulation results and the experimental data is 1.01%, demonstrating good reliability and accuracy.

Under higher pressure, the flow field of the jet presents the shock wave and a recirculation zone structure near the wall surface. Another contrast experiment used Henderson et al.'s[38,39] model to verify the accuracy of the under-expanded jet-impinging structure. Figure 5c,d depicts the experimental

https://doi.org/10.1021/acsomega.3c02751
ACS Omega 2023, 8, 25326−25335

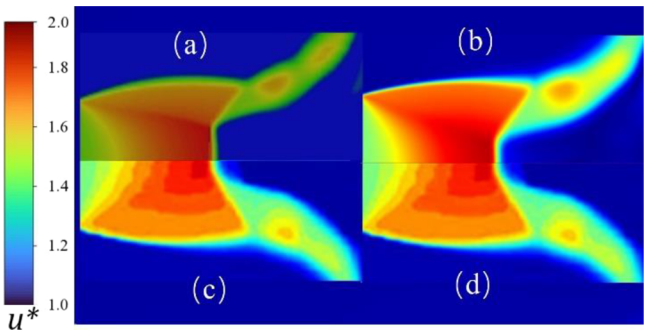

Figure 5. Comparison of the contour patterns of the mean velocity field: (a) simulation result; (b) LES simulation of Cui;[38] (c) experimental result of Henderson et al.;[39] (d) experimental result of Henderson et al.[39] Reprinted in part with permission from ref 39. Copyright 2005 Cambridge University Press.

results of Henderson's experiment, while Figure 5b shows the LES simulation results.[38] The experimental data were obtained by averaging 400 instantaneous fields acquired by digital particle image velocimetry.[39] The LES result was obtained by averaging 500 snapshots of the velocity field saved during the numerical simulation. Figure 5a exhibits the simulation result in this research. The nozzle exits diameter D_Φ = 25.4 mm, and the nozzle-to-wall spacing L_d/D_Φ = 2.08. The nondimensional pressure u^* is the ratio of local velocity to the velocity at the nozzle exit. In the DES simulations, LES is applied to the separation region where large-scale vortices dominate. In contrast, the RANS model is used to deal with the wall boundary layer. Therefore, DES not only captures the fluctuating characteristics of turbulence, while significantly reducing the computational cost significantly compared to LES simulations. The under-expanded structure result shows that the shock waves, recirculation zone, and wall jet positions are consistent with the experiment and the LES simulation. Figure 5 shows that surface shock structures, such as plate shock and tail shock, can be observed in the impinging zone. As the flowing fluid approaches the wall, it experiences plate shock and a severe deceleration of its speed. As a result, recirculating flows appear instead of high-speed jet in the impinging zone. A shear layer forms between the subsonic flow in the central region of the jet behind the Mach disk. A contact surface forms between the recirculation zone and the flow behind the Mach disk. Verifying the above model shows that the model has good accuracy in predicting the fluid−structure near the wall and the impinging pressure of the under-expanded impinging wall.

3.2. Flow Field Structure and the Pressure Distribution at Nozzle-to-Wall Distance L_d/D_Φ = 3. This section investigates the jet impingement flow field and pressure distribution under different NPR conditions. The ambient pressure in the simulation was set at 7.5 MPa, and the dimensionless distances L_d/D_Φ was set at 3. As an initial state, the flow structure of impinging jets was investigated. The CO_2 fluid flows through the nozzle and is accelerated, forming the high-speed jet at the exit. As shown in Figure 6a,b), when the flow field has reached a relative stability state, the instantaneous snapshots and time-averaged velocity contours in the jets' wall for NPR = 2. The flow field has three specific regions, i.e., the free jet region prior to impingement, the impinging zone, and

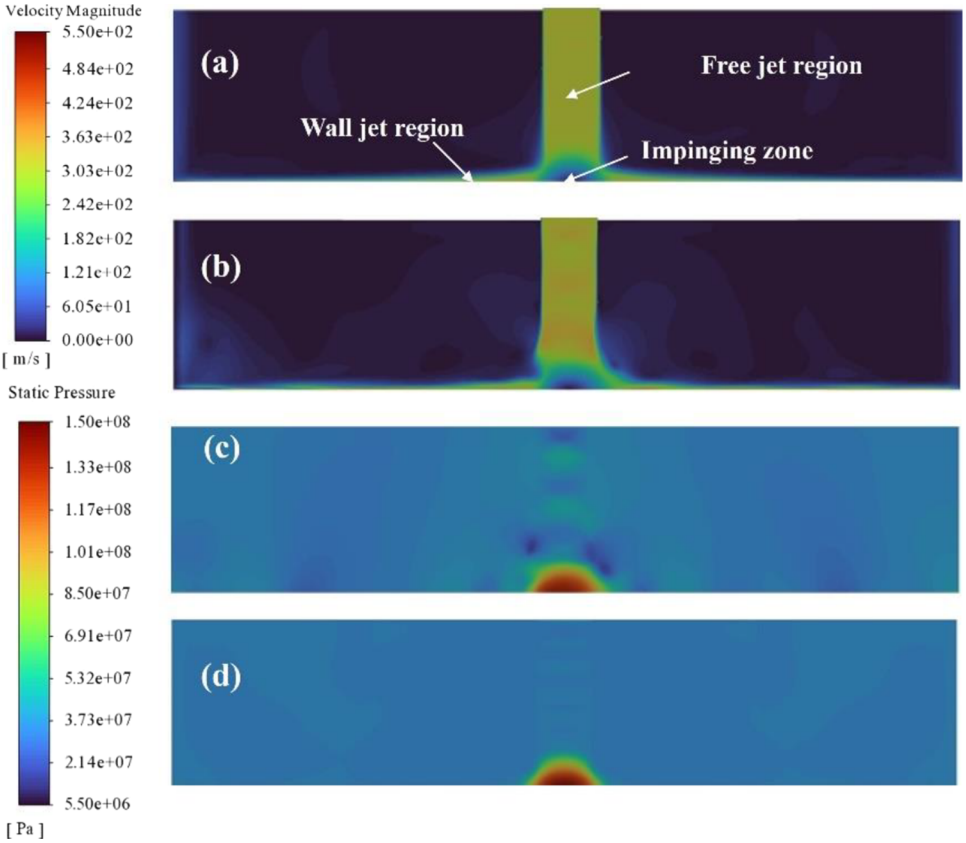

Figure 6. Simulation result of the SC-CO_2 impinging jet (NPR = 2): (a) time-averaged velocity contours; (b) instantaneous snapshots velocity contours; (c) instantaneous snapshots pressure contours *t*; (d) time-averaged pressure contours.

https://doi.org/10.1021/acsomega.3c02751
ACS Omega 2023, 8, 25326−25335

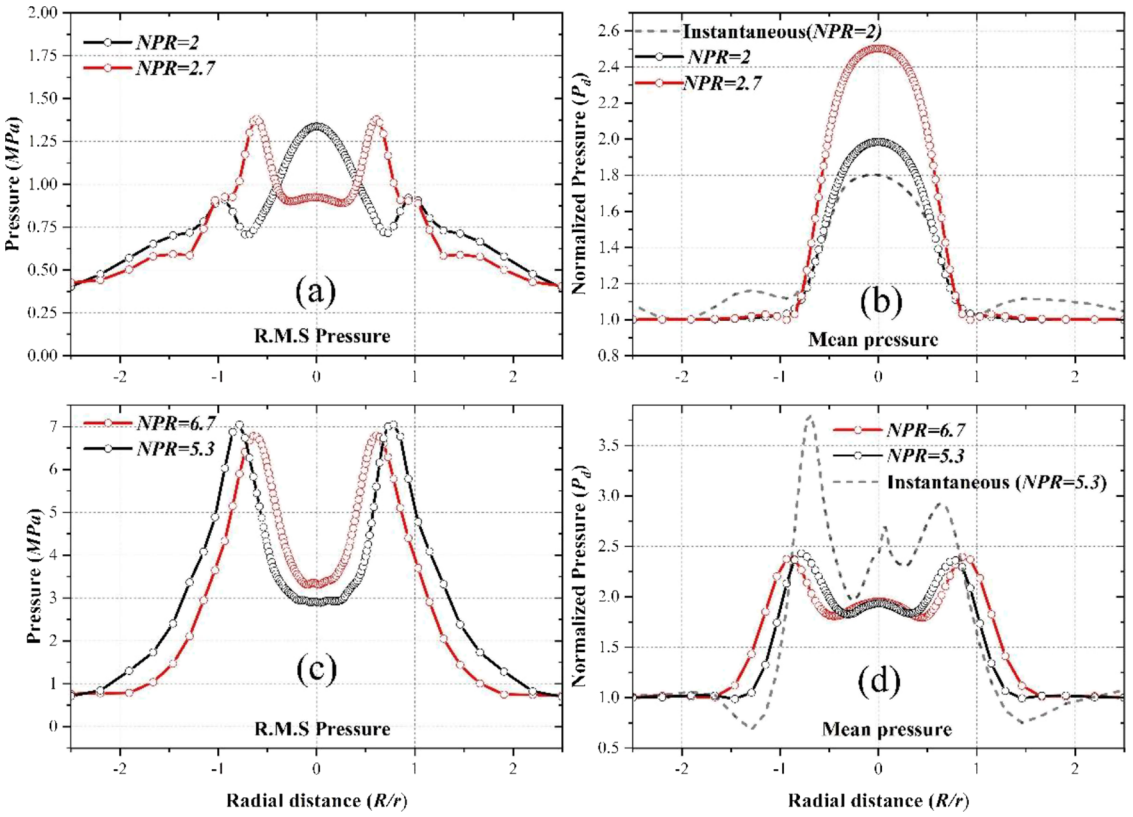

Figure 7. Pressure distribution when $L_d/D_\Phi = 3$; (a) radial profile of dimensionless stagnation pressure when NPR = 2 and 2.7; (b) RMS pressure of the simulation result of the SC-CO_2 impinging jet when NPR = 2 and 2.7; (c) radial profile of dimensionless stagnation pressure when NPR = 5.3 and 6.7; (d) RMS pressure of the simulation result of the SC-CO_2 impinging jet when NPR = 5.3 and 6.7.

the wall jet region 10. The space cannot make a fully developed jet for the low nozzle-to-wall condition in the free jet region. The potential core has a uniform velocity. The wall then interrupts the potential core, while the velocity decreases close to zero. On the impinging surface, the fluid is strongly compressed near the wall. The jet flows dynamic pressure is converted to static pressure, resulting in a high-pressure zone in the central region, as shown in Figure 6c,d. The CO_2 jet impinges the wall, forming a highly dense area in the impinging area. This CO_2 structure continuously produces and impinges the wall surface. Then the stress wave reflected from the wall is superimposed on the CO_2 mass to form a continuous vibration on the wall's surface. In this region, the jet turns toward the radial direction to form a wall jet region. Slight oscillations of the stagnation zone occur in the impinging jet, as shown in Figure 6b. Such oscillations directly determine the pressure fluctuations at the stagnation point and enhance fluctuations in the wall jet region.

The numerical simulation data were extracted and analyzed to clarify the jet-impinging pressure distribution and pressure fluctuations. The results of the pressure distribution of the impinging zone are shown in Figures 7 and 8. It is observed from the figures that the normalized pressure P_d is defined as the ratio of the pressure P to the ambient pressure P_{am}. The jet forms a distinct impinging zone in the central region with a maximum pressure close to the inlet pressure. The pressure distribution on the wall surface exhibits an approximately normal distribution. The dimensionless pressure ratio in the center reaches 1.97, which is close to the nozzle pressure ratio NPR = 2. This result indicates that the SC-CO_2 can maintain a high stagnation pressure and low flow energy loss. The dimensionless radius distance of the impacting jet area is approximately 2. To further

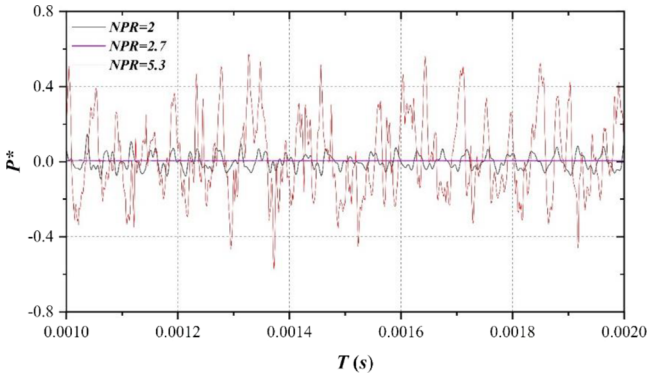

Figure 8. Comparison of the patterns of pressure fluctuations ($L_d/D_\Phi = 3$).

study the dynamic fluctuations of pressure on the impinging surface, the root mean square (RMS) pressure shows the fluctuation of pressure, as shown in Figure 7a. The largest fluctuation area can be seen in the center of the impinging zone. The pressure monitoring point at the stagnation point was set up to monitor the dynamic change of pressure. The nondimensional pressure p^* is the ratio of instantaneous pressure to time-averaged pressure. The result indicates that after a short period of pressure fluctuation, the pressure in the central area stabilizes in a certain range with slight fluctuations, as shown in Figure 10. The dimensionless pressure p^* is less than 0.2 in the whole process. When NPR = 2, the impact pressure in the stagnation region is higher than that in other regions. Smaller pressure

https://doi.org/10.1021/acsomega.3c02751
ACS Omega 2023, 8, 25326−25335

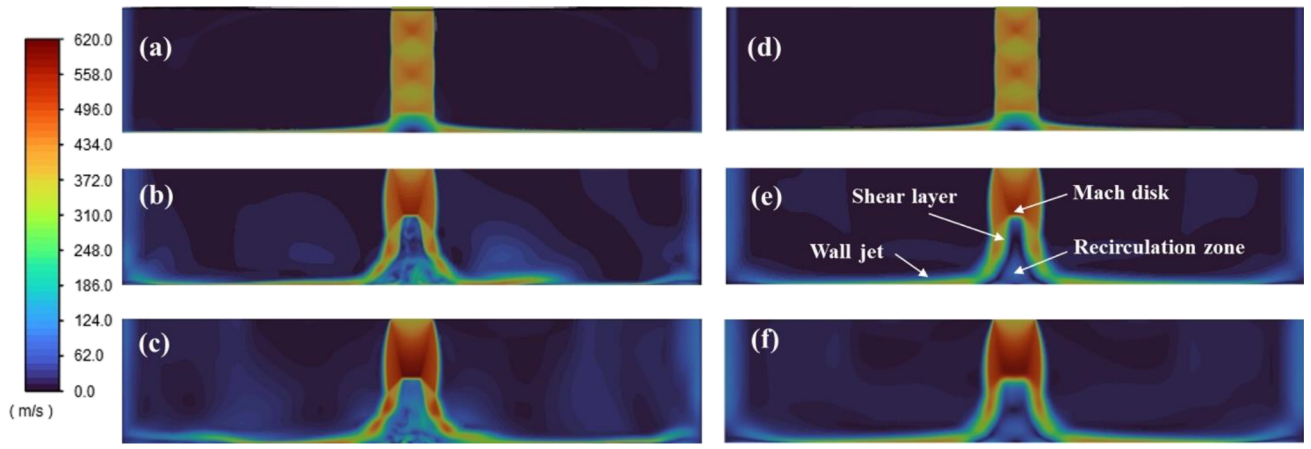

Figure 9. Simulation result of the SC-CO_2 impinging jet: (a) time-averaged velocity contours (NPR = 2.7); (b) instantaneous snapshot velocity contours (NPR = 2.7); (c) time-averaged velocity contours (NPR = 5); (d) instantaneous snapshots velocity contours (NPR = 5); (e) time-averaged velocity contours (NPR = 6.7); (f) instantaneous snapshots velocity contours (NPR = 6.7).

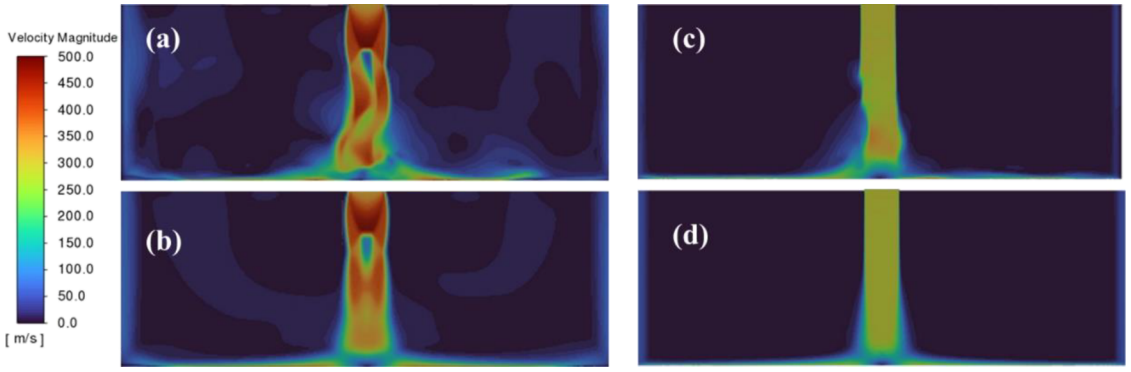

Figure 10. Simulation result of the SC-CO_2 impinging jet: (a) instantaneous snapshots velocity contours (NPR = 2); (b) time-averaged velocity contours (NPR = 2); (c) instantaneous snapshots velocity contours (NPR = 6.7); (d) time-averaged velocity contours (NPR = 6.7).

losses and pressure peak areas can significantly increase the depth of rock-breaking in the central region.

With the increase of the inlet pressure, there is an increase in the degree of expansion after it is ejected from the nozzle. The jet presents a state of under-expansion, and typical alternating expansion waves and compression waves appear in the jet. When NPR = 2.7, the jet boundary of the impinging zone expands outwards, as shown in Figure 9a,d. In the boundary region, the turbulence intensity is increased due to high-velocity gradients between the CO_2 jet and the environment. With increasing pressure from the nozzle, the jet becomes broader. The expansion and compression wave structure will increase the energy loss, increasing the peak stagnation pressure loss of the center. The peak-normalized pressure ratio is 2.51, reaching 92.9% of the inlet pressure ratio, as shown in Figure 7. The expansion wave and compression wave structure caused energy dissipation. Thus, the ratio of wall static pressure to inlet pressure gradually decreased.

The structure of the flow field (NPR = 5.3) is shown in Figure 9b,e. The structure of the flow field shows an under-expanded flow field structure. The simulation result has well reproduced the impinging jet's main features, including the position of the shock waves. During the contraction process, the expanding part of CO_2 is accelerated and ejected from the nozzle exit at supersonic velocity due to the enormous pressure gradient. When the under-expanded SC-CO_2 jet flows out of the nozzle, an expansion wave is formed at the nozzle lip due to the pressure difference. The flow field structure of the impingement jet can generally be divided into several regions according to its flow characteristics, the recirculation region, and the wall jet region. A shear layer forms between the flow in the central region of the jet behind the Mach disc and the supersonic flow in the outer edge area of the jet. The flow near the wall cannot overcome the maximum pressure outboard of the central region and a recirculation zone form close to the wall.

The CO_2 flow was diverted to the shear layer and away from the recirculation zone. In the wall outboard of the central region, the flow passing through the Mach disc is redirected to the shear layer. The CO_2 flow away from the central regions of the jet. The jet flows change direction along the radial flow and is called a wall jet. The pressure lost behind the Mach disc results in low pressure at the center of the wall, a pressure maximum further out near the center, as shown in Figure 7c,d.[39] For the under-expanded jet, it can be seen that there is a significant difference between the pressure distribution in the impinging region and the case of low NPR. The most noticeable feature is that its maximum pressure value is not in the central region for the recirculation zone. There are two peaks near the central region approximately at a distance from the center R/r = 0.8, which have been confirmed by previous experimental studies.[27]

The highest NPR shows a clear Mach disc and outer shear layer, as seen in Figure 10c,f. When the NPR ratio increases to 6.7, the Mach disc is seen to spread to both sides, forming a larger circulation area in the impinging zone. Figure 7 shows the

https://doi.org/10.1021/acsomega.3c02751
ACS Omega 2023, 8, 25326−25335

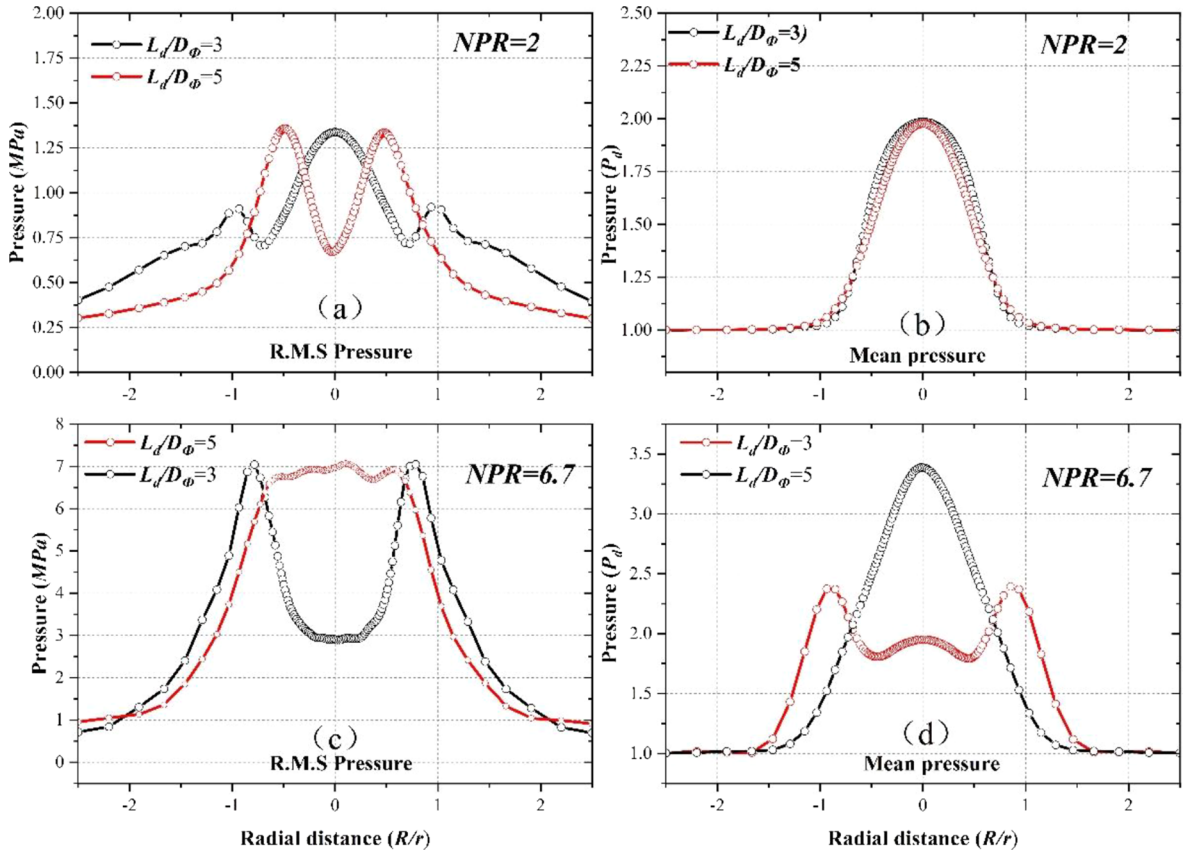

Figure 11. Pressure distribution when $L_d/D_\Phi = 5$: (a) radial profile of dimensionless stagnation pressure when NPR = 2 and 2.7; (b) RMS pressure of the simulation result of the SC-CO_2 impinging jet when NPR = 2 and 2.7; (c) radial profile of dimensionless stagnation pressure when NPR = 5.3 and 6.7; (d) RMS pressure of the simulation result of the SC-CO_2 impinging jet when NPR = 5.3 and 6.7.

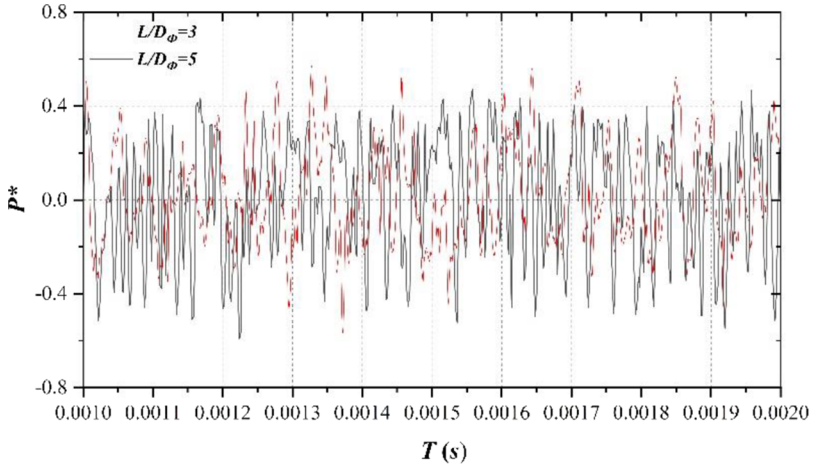

Figure 12. Comparison of the patterns of pressure fluctuations ($L_d/D_\Phi = 5$).

wall pressure distribution under different NPRs. The peak pressure on the surface of the wall does not increase significantly as the NPR increases. The pressure decrease in the central area of the wall was due to the occurrence of a shear layer along the slip surface in the impinging jet. The result from Figure 7 indicate that in the time-averaged pressure distribution, the high-pressure area of the core impinging zone increased by 14.5% compared with $P = 5.3$ (The high-pressure area is defined as: $P_d > 1.5$). When the NPR is equal to 5.3 or 6.7, the jets in different expansion states form multiple pressure centers, which expand the rock-breaking area of the jet and significantly improve the rock-breaking efficiency.

The time-averaged contours of streamwise velocities of the supercritical CO_2 jet at different pressure ratios were obtained, as shown in Figure 9. Oscillations of the stagnation zone that occur in the impinging jet are more intense compared to the condition when NPR = 2 and 2.7 due to shock structure and the vortex ring in the shear layer. The momentum carried by the CO_2 jet affects the pressure distribution also. When the NPR ratio increases to 5.3, significant oscillations are demonstrated in the wall jet as a result of the motion of the recirculation zone in

https://doi.org/10.1021/acsomega.3c02751
ACS Omega 2023, 8, 25326−25335

the internal subsonic flow and the oscillations generated in the compression and expansion zones in the peripheral supersonic flow.

3.3. Flow Field Structure and the Pressure Distribution at Nozzle-to-Wall Distance $L_d/D_\Phi = 5$. This section analyzes the case of the nondimensional nozzle-to-wall distance L_d/D_Φ is 5. Figures 10 and 11 give the velocity and pressure contours from the simulations when the NPR is 2 and 6.7. As the nozzle-to-wall distance increases, the pressure distribution at the impact wall shows different distribution patterns due to the different characteristics of the jet development. For the fully expanded jet (NPR = 2), the pressure in the impinging region decreases by about 4.04% when the normalized impact distance L_d/D_Φ is increased from 3 to 5. Compared to shorter distances, the nozzle is positioned further from the surface, and the impinging jet is fully developed (Figure 12). The radial pressure distribution is more extensive in the radial direction, as shown in Figure 11. The result indicates that in the core impinging area, the impinging area is also slightly expanded, increasing by about 2.7% compared with $L_d/D_\Phi = 3$. At a low-pressure ratio, with the increase of normalized impact distance L_d/D_Φ, the time-average pressure changes slightly, but there are large fluctuations in the imping zone.

As the nozzle-to-wall distance is increased further when the NPR is 6.7, the large space distance provides the full development of the CO_2 jet. In the state of under-expansion, the shear layers extend downstream more when increasing NPR. From the instantaneous snapshot velocity contours, the result shows that the downstream area of the jet swings back and forth in a particular area due to the instability of the shear layer. With the high dimensionless distance L_d/D_Φ, the Mach disc moves downstream, and the diameter of the Mach disc also slightly widens. The influence of downstream feedback on upstream is weakened. The result shows that in the impinging zone, due to the oscillation of the shear layer, a range of impinging zone is formed in the center. Under the large nozzle-to-wall distance, the fluctuation of the shear layer makes the impact pressure also expand the fluctuation range. For the instability of the jet downstream, there is a high average pressure value in the central area. For a certain energy, reducing the energy dissipation during the jet impact is an effective way to improve the jet impact.[8,14] With the nozzle to the target distance increases, the pressure distribution range also increases. The energy dissipation caused by the energy exchange between the flow field and the shear layer is also more obvious, and the effect on the effective impact pressure will be more significant. Determining the appropriate pressure distribution characteristics can effectively improve the efficiency of rock-breaking.

4. CONCLUSIONS

The fluctuation characteristics of the SC-CO_2 jet and the flow field structure were investigated to provide a theoretical support in engineering applications. In this study, a CFD model has been validated compared with the experimental data. A DES model and the real gas EOS were used in the simulation. In addition, the influence of different flow field structures on pressure distribution were mainly studied. The main conclusions are as follows:

1. Overall, the results compare well with experimental data of the literature for jets with similar initial conditions. The flow field structure of the SC-CO_2 jet exhibited different characteristics by the different nozzle pressure ratio NPR, and the flow field structure will affect the pressure distribution and fluctuation characteristics.
2. When NPR = 2, the CO_2 fluid is in a fully expanded state, forming an impinging area on the wall's surface, with the highest pressure close to the stagnation pressure at the inlet and in a relatively stable state. With the increase of the NPR, the fluid presents a typical under-expansion flow field structure. The expansion wave and compression wave structure caused energy dissipation. Thus, the ratio of wall static pressure to inlet pressure gradually decreased.
3. Under the high NPR (NPR = 5.3 and 6.7), the fluid flow structure makes the highest pressure near the center where the dimensionless distance $R/r = 0.8$, forming a return zone at the stagnation point, making the pressure distribution appear annular peak. The high-pressure area of the core impinging zone increased by 14.5%, with NPR from 5.3 to 6.7. At the stagnation point, the pressure fluctuates wildly.
4. Different dimensionless distances L_d/D_Φ have significant effects on the structure and pressure distribution of the flow field. At a lower L_d/D_Φ, its fluctuation increases with pressure. The result indicates that the core impinging area is also slightly expanded, increasing by about 2.7%, and the peak pressure in the center also decreases by about 4.04%. At a higher distance, a larger pressure area appears in the central area.

AUTHOR INFORMATION

Corresponding Author

Zhenjian Liu − *College of Civil Engineering, Yancheng Institute of Technology, Yancheng 221051, China;* orcid.org/0000-0003-4553-5669; Phone: +86-188-752-08316; Email: zjliu@cqu.edu.cn

Authors

Chao Pu − *A Key Lab Low-Grade Energy Utilization Technologies & Systems, Chongqing University, Ministry of Education, Chongqing 400030, PR China*

Ge Pu − *A Key Lab Low-Grade Energy Utilization Technologies & Systems, Chongqing University, Ministry of Education, Chongqing 400030, PR China;* orcid.org/0000-0003-3080-4088

Complete contact information is available at: https://pubs.acs.org/10.1021/acsomega.3c02751

Author Contributions

Conceptualization, C.P. and Z.L.; methodology, C.P.; software, C.P.; validation, C.P., Z.L.; formal analysis, C.P.; investigation, C.P. and G.P.; resources, C.P.; data curation, C.P. and Z.L.; writing original draft preparation, C.P.; writing review and editing, C.P.; visualization, C.P. and G.P.; supervision, Z.L., G.P.; project administration, Z.L.; funding acquisition, C.P., Z.L., and G.P.

Funding

This research was funded by Funding for school-level research projects of Yancheng Institute of Technology (Grant No. xjr2020036).

Notes

The authors declare no competing financial interest.

https://doi.org/10.1021/acsomega.3c02751
ACS Omega 2023, 8, 25326−25335

REFERENCES

(1) Zhang, C. P.; Liu, S.; Ma, Z. Y.; Ranjith, P. G. Combined micro-proppant and supercritical carbon dioxide (SC-CO2) fracturing in shale gas reservoirs: A review. *Fuel* **2021**, *305*, No. 121431.

(2) Chong, Z. R.; Yang, S. H. B.; Babu, P.; Linga, P.; Li, X.-S. Review of natural gas hydrates as an energy resource: Prospects and challenges. *Appl. Energy* **2016**, *162*, 1633−1652.

(3) Hamza, A.; Hussein, I. A.; Al-Marri, M. J.; Mahmoud, M.; Shawabkeh, R.; Aparicio, S. CO2 enhanced gas recovery and sequestration in depleted gas reservoirs: A review. *J. Pet. Sci. Eng.* **2021**, *196*, No. 107685.

(4) Wang, F.; Cao, P.; Wang, Y.; Hao, R.; Meng, J.; Shang, J. Combined effects of cyclic load and temperature fluctuation on the mechanical behavior of porous sandstones. *Eng. Geol.* **2020**, *266*, No. 105466.

(5) Ghanizadeh, A.; Bhowmik, S.; Haeri-Ardakani, O.; Sanei, H.; Clarkson, C. R. A comparison of shale permeability coefficients derived using multiple non-steady-state measurement techniques: Examples from the Duvernay Formation, Alberta (Canada). *Fuel* **2015**, *140*, 371−387.

(6) Zhang, H.; Liu, Y.; Tang, J.; Liu, W.; Chen, C. Investigation on the fluctuation characteristics and its influence on impact force of supercritical carbon dioxide jet. *Energy* **2022**, *253*, No. 124125.

(7) Zhou, Z.; Lu, Y.; Tang, J.; Zhang, X.; Li, Q. Numerical simulation of supercritical carbon dioxide jet at well bottom. *Appl. Therm. Eng.* **2017**, *121*, 210−217.

(8) Tian, S.; He, Z.; Li, G.; Wang, H.; Shen, Z.; Liu, Q. Influences of ambient pressure and nozzle-to-target distance on SC-CO2 jet impingement and perforation. *J. Nat. Gas Sci. Eng.* **2016**, *29*, 232−242.

(9) Chen, C.; Liu, Y.; Tang, J.; Wang, W. Investigation of Coal Failure Characters Based on Jet Energy and Impact Frequency During Particle Jets Coal Breaking. *Rock Mech. Rock Eng.* **2022**, *55*, 4109−4122.

(10) Li, X.; Si, K.; He, T.; Li, C. Dynamic Effect of Shaped Charge Blasting and Its Application in Coal Seam Permeability Enhancement. *ACS Omega* **2022**, *7*, 25353−25365.

(11) Long, X.; Liu, Q.; Ruan, X.; Kang, Y.; Lyu, Q. Numerical investigation of the flow of supercritical carbon dioxide injected into the bottom hole during drilling with special emphasis on the real gas effects. *J. Nat. Gas Sci. Eng.* **2016**, *34*, 1044−1053.

(12) Li, M.; Ni, H.; Cao, Y.; Zhao, B.; Lei, P.; Shi, X.; Du, Y. Flow energy transformation and dissipation mechanisms of carbon dioxide, nitrogen, and water jets. *J. Nat. Gas Sci. Eng.* **2020**, *84*, No. 103650.

(13) Cai, C.; Kang, Y.; Wang, X.; Hu, Y.; Chen, H.; Yuan, X.; Cai, Y. Mechanism of supercritical carbon dioxide (SC-CO2) hydro-jet fracturing. *J. CO2 Util.* **2018**, *26*, 575−587.

(14) Liu, Y.; Guo, X.; Wei, J.; Zhang, H. Application of supercritical carbon dioxide jet: A parametric study using numerical simulation model. *J. Pet. Sci. Eng.* **2021**, *201*, No. 108422.

(15) Cai, C.; Kang, Y.; Yang, Y.; Liao, F.; Chen, Y.; Huang, M.; Chen, H. Experimental investigation on flow field and induced strain response during SC-CO2 jet fracturing. *J. Pet. Sci. Eng.* **2020**, *195*, No. 107795.

(16) Cai, C.; Kang, Y.; Yang, Y.; Wang, X.; Li, Y.; Huang, M.; Wu, J. The effect of shale bedding on supercritical CO2 jet fracturing: A experimental study. *J. Pet. Sci. Eng.* **2020**, *195*, No. 107798.

(17) Yan, H.; Zhang, J.; Zhou, N.; Li, M.; Suo, Y. Numerical simulation of dynamic interactions between two cracks originating from adjacent boreholes in the opposite directions during supercritical CO2 fracturing coal mass. *Eng. Fract. Mech.* **2020**, *223*, No. 106745.

(18) Liu, Y.; Zhang, J.; Wei, J.; Wang, C.; Cui, J. Impact pressure distribution of an SC-CO2 jet used in rock breakage. *Geomech. Geophys. Geo-Energy Geo-Resour.* **2022**, *8*, No. 27.

(19) Song, X.; Lyu, Z.; Li, G.; Sun, B. Model evaluation and experimental validation of thermal jet drilling for geothermal energy. *Geothermics* **2019**, *77*, 151−157.

(20) Limaye, M. D.; Gulati, P.; Vedula, R. P.; Prabhu, S. V. Effect of the profile of a convergent nozzle on heat transfer distribution of a flat plate impinged by an under-expanded jet. *Exp. Therm. Fluid Sci.* **2013**, *45*, 75−91.

(21) Kuo, C.-Y.; Dowling, A. P. Oscillations of a moderately underexpanded choked jet impinging upon a flat plate. *J. Fluid Mech.* **2006**, *315*, 267−291.

(22) Kubacki, S.; Rokicki, J.; Dick, E. Hybrid RANS/LES computations of plane impinging jets with DES and PANS models. *Int. J. Heat Fluid Flow* **2013**, *44*, 596−609.

(23) Tummers, M. J.; Jacobse, J.; Voorbrood, S. G. J. Turbulent flow in the near field of a round impinging jet. *Int. J. Heat Mass Transfer* **2011**, *54*, 4939−4948.

(24) Zhang, X.; Lu, Y.; Tang, J.; Zhou, Z.; Li, Q. Dynamic simulation of the oscillation characteristics of supercritical carbon dioxide impacting jets. *J. Vib. Control* **2019**, *25*, 61−71.

(25) Yadav, K. R.; Paul, A. R.; Jain, A. Performance evaluation of a twin air-intake: effects of geometry, Reynolds number and jet momentum coefficient. *Eur. Phys. J. Plus* **2021**, *136*, 988.

(26) Rhea, S.; Bini, M.; Fairweather, M.; Jones, W. P. RANS modelling and LES of a single-phase, impinging plane jet. *Comput. Chem. Eng.* **2009**, *33*, 1344−1353.

(27) Yaga, M.; Ueda, K.; Ohshiro, T.; Senaha, I.; Oyakawa, K. Experimental and Three-Dimensional Numerical Study on Under-Expanded Impinging Jets. *J. Therm. Sci.* **2000**, *9*, 316.

(28) Chin, C.; Li, M.; Harkin, C.; Rochwerger, T.; Chan, L.; Ooi, A.; Risborg, A.; Soria, J. Investigation of the Flow Structures in Supersonic Free and Impinging Jet Flows. *J. Fluids Eng.* **2013**, *135*, No. 031202.

(29) Elshahomi, A.; Lu, C.; Michal, G.; Liu, X.; Godbole, A.; Venton, P. Decompression wave speed in CO2 mixtures: CFD modelling with the GERG-2008 equation of state. *Appl. Energy* **2015**, *140*, 20−32.

(30) Wang, X.; Song, Z.; Pan, X.; Zhang, L.; Zhu, X.; Mei, Y.; Jiang, J. Simulation study on near-field structure and flow characteristics of high-pressure CO2 released from the pipeline. *J. Loss Prev. Process Ind.* **2021**, *71*, No. 104481.

(31) Liu, X.; Godbole, A.; Lu, C.; Michal, G.; Venton, P. Source strength and dispersion of CO2 releases from high-pressure pipelines: CFD model using real gas equation of state. *Appl. Energy* **2014**, *126*, 56−68.

(32) Wu, X.; Huang, Z.; Dai, X.; McLennan, J.; Zhang, S.; Li, R. Detached eddy simulation of the flow field and heat transfer in cryogenic nitrogen jet. *Int. J. Heat Mass Transfer* **2020**, *150*, No. 119275.

(33) Kubacki, S.; Rokicki, J.; Dick, E. Predictions of round impinging jet heat transfer with two k−ω hybrid RANS/LES models. *Int. J. Numer. Methods Heat Fluid Flow* **2013**, *23*, 1023−1048.

(34) Gojon, R.; Bogey, C. Flow Features near Plate Impinged by Ideally Expanded and Underexpanded Round Jets. *AIAA J.* **2018**, *56*, 445−457.

(35) Raman, S. K.; Kim, H. D. Solutions of supercritical CO2 flow through a convergent-divergent nozzle with real gas effects. *Int. J. Heat Mass Transfer* **2018**, *116*, 127−135.

(36) Wang, C.; Li, Y.; Teng, L.; Gu, S.; Hu, Q.; Zhang, D.; Ye, X.; Wang, J. Experimental study on dispersion behavior during the leakage of high pressure CO2 pipelines. *Exp. Therm. Fluid Sci.* **2019**, *105*, 77−84.

(37) Span, R. W.; Wagner, W. A New Equation Of State for Carbon Dioxide Covering the Fluid Region from the Triple-Point Temperature to 1100 K At Pressures up to 800 MPa. *J. Phys. Chem. Ref. Data* **1996**, *25*, 1509−1596.

(38) Cui, W.; Xu, J.; Wang, B.-C.; Zhang, P.; Qin, Q. The initial flow structures and oscillations of an underexpanded impinging jet. *Aerosp. Sci. Technol.* **2021**, *115*, No. 106740.

(39) Henderson, B.; Bridges, J.; Wernet, M. An experimental study of the oscillatory flow structure of tone-producing supersonic impinging jets. *J. Fluid Mech.* **2005**, *542*, 115.

https://doi.org/10.1021/acsomega.3c02751
ACS Omega 2023, 8, 25326−25335